Vortex generation in stirred binary Bose-Einstein condensates

Anacé N. da Silva [1,*] R. Kishor Kumar,[2,†] Ashton S. Bradley,[2,‡] and Lauro Tomio [1,§]

[1]*Instituto de Física Teórica, Universidade Estadual Paulista, 01140-070 São Paulo, SP, Brazil*

[2]*Department of Physics, Centre for Quantum Science, and Dodd-Walls Centre for Photonic and Quantum Technologies, University of Otago, Dunedin 9054, New Zealand*

Binary Bose-Einstein condensates of two distinct atomic species are studied, with interesting effects being verified due to the imbalance of atomic masses. We study the formation of vortices and associated turbulence flows created by stirring two mass-imbalanced coupled Bose-Einstein condensates in the miscible regime. We consider the mixture in the laboratory frame, confined in a pancake-like harmonic trap slightly perturbed elliptically by a time-dependent periodic potential, which introduces turbulent dynamics with final stable patterns of vortices, induced by the periodicity of the perturbation. Derived rotational frequencies are shown to be associated with the observed vortex patterns in the asymptotic regime, with a correspondence between the stirring procedure and a direct time-independent approach being indicated. It was also confirmed that a larger pattern of vortices is supported by the higher mass condensed species at the same frequency. For the experimentally accessible mixtures ^{85}Rb - ^{133}Cs and ^{85}Rb - ^{87}Rb, we numerically solve the equations of motion and analyze the system dynamics using a range of measures including energy spectra. In the transient turbulent regime, spectral analysis shows evidence for the characteristic $k^{-5/3}$ Kolmogorov classical law associated with turbulence, modified by the universal k^{-3} vortex core scaling in the ultraviolet regime.

I. INTRODUCTION

The experimental observations of vortices in Bose-Einstein condensates (BECs) [1–8] have been motivated by looking at their predicted relevance to fundamental aspects of quantum mechanics, such as superfluidity, which was previously verified in rotating superfluid of helium, with the formation of vortex arrays [9] (see Refs. [10–12] for reviews). The theoretical and experimental investigations related to the dynamical formation of vortices in BECs, as well as the induced mechanisms to generate them, are outlined in several reviews [13–17], which describe the advances following the first experiments. Techniques such as rotating the magnetic trap, laser stirring, and oscillating excitation superimposing the trapping potential have been used to nucleate vortices in BECs [2,3,17].

Concepts of fluid turbulence were applied to rotating BECs by considering a weak time-dependent elliptical deformation of the confining potential [18]. The deformation generates turbulent flow via quadrupole instability. Energy injected during the instability is damped by vortex-sound interactions and particle loss, and a vortex lattice forms at long times in equilibrium with the drive. The classical and quantum regimes of two-dimensional turbulence produced in trapped BECs have been studied in a number of works [19–23], using spectral

analysis that decomposes the kinetic energy into compressible (sound) and incompressible (vortex) components; see Refs. [24–26] for reviews of the maturing field of quantum turbulence in quantum gases.

More recently, the fundamental differences between quantum and classical turbulence in rotating systems have been investigated [27]. In binary systems, recent studies have considered vortex dynamics leading to pattern formation [28,29], motivating further study to understand vortex mechanisms and their relation with sound-wave excitations [30,31]. In a disordered two-dimensional (2D) turbulent quantum fluid, the emergence of high-energy coherent vortex structures has been observed in simulations [21], consistent with recent experiments [23]. Three-dimensional structures of vortices have also been studied in dipolar BECs, by considering fully anisotropic traps, with increasing eccentricity [32].

The production of vortices in multicomponent BECs is more intriguing due to the diverse vortex lattice phases, which can be observed in addition to the more fundamental Abrikosov triangular kind of patterns first predicted in type II superconductors [33–35]. See Ref. [36] for a more recent overview of vortex lattice theory focusing on experiments in Bose-Einstein condensates. With two different hyperfine states of the same rubidium isotope, ^{87}Rb, the first production of two overlapping BECs [37] was followed by studies on collective oscillations of two colliding BECs [38] and investigations of atomic and molecular properties of coupled BECs [39].

For two different isotopes of rubidium, ^{85}Rb and ^{87}Rb, existing theory already indicates that a stable mixed-isotope double condensate could be formed by sympathetic

*anace.nunes@unesp.br

†kishor.bec@gmail.com

‡ashton.bradley@otago.ac.nz

§lauro.tomio@unesp.br

evaporative cooling, allowing partial control of the interactions between hyperfine states [40], and was followed quickly by the experimental production of potassium-rubidium (^{41}K and ^{87}Rb) condensed coupled mixture [41]. Their collisional properties were further studied [42], including control of the interspecies interactions [43]. Observation of controllable phase separation [44] was followed by production of ^{87}Rb and ^{133}Cs coupled BECs [45], strontium isotopes ^{84,88}Sr [46], potassium ^{39}K [47], and sodium ^{23}Na [48]. Strongly dipolar ultracold gases of dysprosium (Dy) and erbium (Er) [49,50] led to several new works on dipolar mixtures.

High experimental control of two-component coupled binary systems suggests the possibility of rotating BECs in atomic mixtures. Such studies have mainly been concentrated on ground-state vortex structures regarding miscibility, which is a relevant characteristic of multicomponent ultracold gases. Their miscible behavior depends on the nature of the interatomic interactions between different species. Miscible or immiscible two-component BECs can be distinguished by the spatial overlap or separation of the respective wave functions of each component. For different binary trapped dipolar mixtures, some rotational properties have been established, for example, in Refs. [51–54]. Following that, the miscible-immiscible transition of dipolar BEC mixtures with vortices was studied within pancake- and cigar-type geometries, by considering dysprosium (^{162,164}Dy) and erbium (^{168}Er) isotopes. Following studies exploring occurrences of vortex patterns in rotating binary mixtures [55,56], the mass-imbalance sensitivity of dipolar mixtures was pointed out in Ref. [57], along with the role of dipole-dipole interactions in causing phase separations.

In the present work, our aim is to analyze the route to vortex generation and stabilization in stirred mass-imbalanced binary BECs. As exemplar systems, we study the two experimentally accessible BEC mixtures ^{85}Rb-^{133}Cs and ^{85}Rb-^{87}Rb, which allow us to distinguish mass-imbalance effects. To understand the process of vortex generation, we analyze the kinetic energy decomposition into compressible and incompressible parts for both components of the mixture. We take extra care to remove rigid body rotation effects on the kinetic energy spectra by computing an instantaneous average rotational frequency in which the analysis can be affected without artifact.

The following Sec. II is split into four parts, with details of the mean-field formalism given in Sec. II A. In Sec. II B we have a description of the parameters and numerical approach. In Sec. II C, the time-dependent energetic relations for the stirring model are given with an analysis of vortex formation. The formalism concerned with the kinetic energy spectra in the rotating-frame field is included in Sec. II D. In Secs. III and IV, we have the main results, where relevant aspects due to mass differences in the mixtures are discussed concerning the vortex patterns and energetic distribution. Section III provides details on the time evolution of observables related to the two kinds of mass-imbalanced coupled systems we are studying, considering the stirring potential. The final vortex pattern results are also compared with ground-state results, obtained without the stirring potential, but assuming the corresponding classical rotational frequency. In Sect. IV, we perform an analysis related to the kinetic energy spectra, with the main focus

concerned with the behavior of the incompressible kinetic energy spectra during the time evolution, before the nucleation of vortices until the time region when stable vortex patterns are established. Finally, in Sec. V we present a summary with our general conclusions and perspectives.

II. STIRRED BOSE-EINSTEIN CONDENSATES

In our present approach, we assume a binary coupled system, in which the two atomic species $i = 1, 2$ have non-identical masses m_i. We further assume that both species have an identical number of atoms $N_i \equiv N$ and are confined by strongly pancake-shaped harmonic traps, with longitudinal and transversal frequencies given, respectively, by $\omega_{i,z}$ and $\omega_{i,\perp}$, with fixed aspect ratios given by $\lambda \equiv \lambda_i = \omega_{i,z}/\omega_{i,\perp} = 10$. As our study will be mainly concerned with the analysis of the dynamic occurrence of vortices in an originally stable miscible binary system, the intraspecies scattering lengths are assumed to be fixed and identical, $a_{11} = a_{22} = 60a_0$ (where a_0 is the Bohr radius), such that the relative strength is controlled by the interspecies scattering length a_{12}. Also, to guarantee that the coupled system is in a miscible state, we assume $a_{12}/a_{ii} = 1/2$, the interspecies interaction being about half of the intraspecies ones. These assumptions related to the nonlinear interactions rely on the actual experimental possibilities to control the interactions via Feshbach resonance mechanisms [58].

The coupled Gross-Pitaevskii (GP) equation is cast in a dimensionless format, with the energy and length units given, respectively, by $\hbar\omega_\rho$ and $\ell_\rho \equiv \sqrt{\hbar/(m_1\omega_\rho)}$, in which we are assuming the first species (the less-massive one) as our reference in our unit system, such that $\omega_\rho \equiv \omega_{1,\perp}$ Correspondingly, the full-dimensional space **r** and time t variables are, respectively, replaced by dimensionless ones. For convenience, we kept the same representation, $\mathbf{r}/\ell_\rho \to \mathbf{r}$ and $\omega_\rho t \to t$, with the new variables understood as dimensionless. Within these units, for simplicity, we first adjust the confining trap frequencies of both species with $m_2\omega_{2,\perp}^2 = m_1\omega_\rho^2$, such that the dimensionless nonperturbed three-dimensional (3D) traps for both species can be represented by the same expression, given by

$$V_{i,3D}(\mathbf{r}) = \tfrac{1}{2}(x^2 + y^2 + \lambda^2 z^2) \equiv V_0(x, y) + \tfrac{1}{2}\lambda^2 z^2, \quad (1)$$

where $V_0(x, y)$ is the 2D harmonic trap. In this way, there is no explicit mass-dependent factor in the trap potential, which will remain only in the kinetic energy term. By fixing to very large values the aspect ratio λ, we can follow the usual approximation, in which we have the factorization of the total 3D wave function, $\psi_i(x, y, t)\chi_i(z)$, with $\chi_i(z) \equiv (\lambda_i/\pi)^{1/4}e^{-\lambda_i z^2/2}$. In this case, the ground-state energy for the harmonic trap in the z direction becomes a constant factor to be added to the total energy. It is safe to assume a common mass-independent transversal wave function for both components, with $\lambda_i = \lambda$, as any possible mass dependence can be absorbed by changing the corresponding aspect ratio. This approach for the reduction to 2D implies that we also need to alter the nonlinear parameters accordingly, as the integration on the z direction will bring us a λ dependence in the nonlinear parameters.

A. Gross-Pitaevskii equations

Motivated by some previous studies, in which single condensed atomic species have been submitted to stirring potentials [2,6,7], in our approach we assume binary coupled condensates, in which both components are confined in pancake-like harmonic traps affected by laboratory-frame time-dependent stirring potentials, represented by identical elliptical trap perturbations oscillating in both x and y directions, as the one considered in Ref. [18]. So, the assumed expression for the 2D time-dependent stirring potential is given by

$$V_s(x, y, t) = \frac{\epsilon}{2}[(x^2 - y^2)\cos(2\Omega_E t) - 2xy \sin(2\Omega_E t)], \quad (2)$$

where Ω_E (given in units of ω_ρ) is the laser stirring frequency parameter, with ϵ the corresponding strength. With the harmonic trap $V_0(x, y)$ perturbed by $V_s(x, y, t)$, the corresponding dimensionless coupled 2D GP equation can be written as

$$i\frac{\partial \psi_i}{\partial t} = \left[\frac{-m_1}{2m_i}\nabla^2 + V_0(x, y) + V_s(x, y, t) + \sum_j g_{ij}|\psi_j|^2\right]\psi_i, \quad (3)$$

where the two-component wave functions, $\psi_i \equiv \psi_i(x, y, t)$, are normalized to one, $\int_{-\infty}^{\infty} dx \int_{-\infty}^{\infty} dy\, |\psi_i|^2 \equiv \int d^2r\, |\psi_i|^2 = 1$, with $-i\nabla \equiv -i(\hat{e}_x\frac{\partial}{\partial x} + \hat{e}_y\frac{\partial}{\partial y})$ being the 2D momentum operator. The parameters g_{ij} are the two-body contact interactions, related to the intra- and interspecies two-body scattering lengths (respectively, a_{ii} and a_{12}), which are given by

$$g_{ij} \equiv \sqrt{2\pi\lambda}\frac{m_1 a_{ij} N_j}{\mu_{ij}\ell_\rho}, \quad (4)$$

where $\mu_{ij} \equiv m_i m_j/(m_i + m_j)$ is the reduced mass. In the next, for our numerical simulations, the length unit will be adjusted to $\ell_\rho = 1\,\mu m \approx 1.89 \times 10^4 a_0$, such that a_{ij} can be conveniently expressed in terms of a_0. The total trap interaction, given by Eqs. (1) and the time-dependent perturbation (2), can also be written in polar coordinates, whenever convenient, with $x = r\cos\theta$, $y = r\sin\theta$ ($0 \leqslant r < \infty$, $0 \leqslant \theta \leqslant 2\pi$), and $r^2 \equiv x^2 + y^2$. Within these coordinates, assuming a stirring potential with identical form for both components, the total trap potential, $V_0(x, y) + V_s(x, y, t)$, can be written as

$$V(r, \theta, t) = \frac{r^2}{2}[1 + \epsilon\, \cos(2\theta + 2\Omega_E t)]. \quad (5)$$

So, the usual trap interaction is affected by a small perturbation, which we assume has strength $\epsilon = 0.025$ (as in Ref. [18]) to maintain the condensates with approximate symmetric 2D shape during the evolution, following some experimental realizations with anharmonic potentials [2,6]. This small periodic perturbation serves to trigger the dynamics by affecting the axial angular position θ. The full trapped strength oscillates between $1 - \epsilon$ and $1 + \epsilon$ (in half period $T = \pi/\Omega_E$), implying that, averaging in a long time interval, it does not change the strength of the trap. However, the stirring frequency has the role to trigger the dynamics, which go through different stages, provoking turbulence, with a final pattern of vortices being formed. So, the time-dependent stirring approach induces asymptotically a rotation in the trap, but differs from an approach in which the rotating frame trap rotation is directly

obtained by applying the angular momentum operator in the ground state.

With the above stirred trap potential applied to the coupled condensates, the dynamical process starts with energy injected into the condensates, exciting a quadrupolar mode oscillation. The full dynamical process relies on the appropriate perturbed frequency Ω_E of the elliptical small perturbation, which should be close to a quadrupole resonance when the amplitude of the oscillations becomes enough large. By changing Ω_E to values where the quadrupole oscillations have reduced amplitude, the system turns out to be stable. Therefore, in this dynamical process the excitation mimics rotation yet the system remains irrotational, as noticed in Ref. [18].

As we are concerned only with the vortex pattern formations, without the time-dependent perturbation, we also consider an independent approach by going to the rotating frame with direct trap rotation, applying the angular momentum operator in the ground-state wave function. In practice, the GP formalism (3) has the following change:

$$V_s(x, y, t) \rightarrow \Omega_0 L_z = -i\Omega_0\frac{\partial}{\partial \theta}. \quad (6)$$

This model serves the purpose of verifying the correspondence between the asymptotic classical rotational frequency obtained from the stirring model and a direct time-independent approach for the vortex pattern productions. As it will be shown, similar patterns are produced in the quantum fluid, with a rotating frame frequency $\Omega_0 < 1$, which can be associated with the asymptotic classical rotational frequency.

In our present study, we have mass-imbalanced coupled condensed systems, such that the full dynamics is expected to be more complex within the stirring mechanism, taking longer than in the single condensed case to reach the final stage, with stable configurations of vortices in both condensates. Beyond the dynamics, which is verified by the interaction between the inner and outer cloud densities of a single condensed system, we additionally have the coupling between two mass-imbalanced condensates. In the stirred trap (5), common for both coupled condensates, after assuming that a small value $\epsilon = 0.025$ for the strength of the perturbation, within our numerical simulations, we search for the appropriate parameter Ω_E to trigger the dynamics in such a way that in the long time interval it can produce stable vortex pattern configurations in each of the condensed clouds. For that it was found that Ω_E needs to be larger than 0.9, with $\Omega_E = 1.25$ being fixed when considering a pattern with nearly 10 or more vortices. This reflects that a smaller effective trap rotation is induced asymptotically in the trap, with Ω_E being just a frequency parameter in the small time-dependent perturbation, generating a quadrupole instability necessary to initiate and maintain the dynamics. As no damping is assumed in the formalism, all the produced kinetic energies are transferred to the production of sound waves (compressible part) and vorticity (incompressible part), as it will be shown. Therefore, we first explore the full dynamics provided by Eq. (3) with the elliptically deformed time-dependent perturbation (5), in which a given laser frequency induces the dynamics in the coupled system, going through different regimes in the long-time evolution to reach stable patterns of vortices. Next, by considering the results obtained with the stirring potential model, we follow a

semiclassical analysis for the relevant rotational observables, in order to define an effective classical frequency Ω_{cl}, which was obtained by time averaging. So, with $\Omega_0 = \Omega_{cl}$, by going to the rotating frame without the time-dependent perturbation, an approximate correspondence was established between both approaches to generate similar vortex patterns.

B. Numerical approach and parameters

In our approach to reach the numerical results presented in the next sections, we solve the 2D coupled GP mean-field equation by the split time-step Crank-Nicolson method, with an appropriate algorithm for discretization as prescribed in Ref. [59]. Within our dimensionless units, in which the time unit is the inverse of the transversal trap frequency $1/\omega_\rho$ and the length unit is $\ell_\rho = \sqrt{\hbar/(m_1\omega_\rho)} = 1$ μm, we consider the space step sizes as 0.05, with time steps 10^{-4}. This space-time discretization was found with enough smaller steps to provide stable results along the time evolution of the coupled system. The space steps are more than four times smaller than the healing lengths, which are the cutoff lengths at the vortex core sizes.

With the binary mixture considered in a completely miscible state, with identical intraspecies scattering lengths ($a_{11} = a_{22}$), the miscibility parameter $\delta \equiv a_{12}/a_{11}$ must be smaller than 1. For that, we assume that both intraspecies scattering lengths are repulsive, with $a_{ii} = 60a_0$ being twice the interspecies one $a_{12} = 30a_0$, such that $\delta = 0.5$. We also consider both species with an identical number of atoms, $N_1 = N_2 = 10^4$. With these parameters, we observe that the miscible-state condition $\delta = 0.5$ will correspond to g_{12}/g_{11}, given by (4), slightly smaller due to the mass differences of the considered binary systems.

The healing lengths are associated with the dimensionless chemical potentials μ_i (units $\hbar\omega_\rho$), which are obtained from the stationary solutions, $\psi_i = \sqrt{n_i}e^{-i\mu_i t}$, given by Eq. (3) with $V_s = 0$. So, with energies in units of $\hbar\omega_\rho$, the healing lengths are in units of $\ell_\rho = 1$ μm, with the speed of sound in units of $\ell_\rho\omega_\rho$. For the binary mixture ^{85}Rb-^{133}Cs, the respective chemical potentials are $\mu_1 = \mu_{85\text{Rb}} = 15.10$ and $\mu_2 = \mu_{133\text{Cs}} = 12.87$. Correspondingly, the healing lengths ξ_i and sound velocities v_i are $\xi_1 = \xi_{85\text{Rb}} = 0.257$, $\xi_2 = \xi_{133\text{Cs}} = 0.223$, $v_{s,1} = v_{85\text{Rb}} = 3.43$, and $v_{s,2} = v_{133\text{Cs}} = 3.71$. In the case of the almost identical mass mixture, ^{85}Rb-^{87}Rb, these values are given by $\mu_1 = \mu_{85\text{Rb}} = 15.53$, $\mu_2 = \mu_{87\text{Rb}} = 15.40$, $\xi_1 = \xi_{85\text{Rb}} = 0.254$, $\xi_2 = \xi_{87\text{Rb}} = 0.252$, and $v_1 = v_{85\text{Rb}} \approx v_2 = v_{87\text{Rb}} = 4.04$. Notice that, due to our choice of units based on the first component, the corresponding full-dimensional expressions of the healing lengths are given by $\tilde{\xi}_i = \ell_\rho\sqrt{m_1/(m_i\mu_i)} \equiv \ell_\rho\xi_i$, with the second component carrying a mass factor in relation to the chemical potential.

C. Analysis of vortex formation

In general, quantum gases are compressible fluids such that their corresponding density can change when submitted to a force. This is true to a certain degree, as part of the fluid can behave as an incompressible fluid, similar to a liquid. In our present case, the condensate is submitted to a time-dependent stirring potential, associated with a torque, which is mainly

due to the compressible part of the kinetic energy. Therefore, for the analysis of this behavior, we start by considering the total energy, in which only the harmonic trap with the time-dependent stirring potential is assumed for the total trap potential, in Eq. (3). So, for each component of the mixture, the total energies $E_i(t)$ are given by

$$E_i(t) = \int d^2\mathbf{r}\left[\frac{m_1}{2m_i}|\nabla\psi_i|^2 + V_i(x,y,t)n_i(x,y,t)\right]$$
$$+ \frac{1}{2}\sum_{j=1,2} g_{ij}\int d^2\mathbf{r}\, n_i(x,y,t)n_j(x,y,t), \quad (7)$$

where $n_{i=1,2}(x,y,t) \equiv |\psi_i|^2$ are the respective time-dependent densities. For each species, with the current densities $\mathbf{j}_i(x,y,t)$ expressed in terms of the respective densities and velocity fields $\mathbf{v}_i(x,y,t)$, such that $\mathbf{j}_i(x,y,t) = n_i\mathbf{v}_i(x,y,t)$, we can write

$$\mathbf{v}_i(x,y,t) = \frac{1}{2i\,|\psi_i|^2}[\psi_i^\star\nabla\psi_i - \psi_i\nabla\psi_i^\star]. \quad (8)$$

The associated kinetic energies,

$$E_i^K(t) = \frac{m_1}{2m_i}\int d^2\mathbf{r}\, n_i(x,y,t)|\mathbf{v}_i(x,y,t)|^2, \quad (9)$$

can be decomposed in compressible $E_i^c(t)$ and incompressible $E_i^{nc}(t)$ parts. For that, the component i of the density-weighted velocity field, defined as $\mathbf{u}_i(x,y,t) \equiv \sqrt{n_i(x,y,t)}\mathbf{v}_i(x,y,t)$, can be split into an incompressible part, $\mathbf{u}_i^{(nc)} \equiv \mathbf{u}_i^{(nc)}(x,y,t)$ satisfying $\nabla\cdot\mathbf{u}_i^{(nc)} = 0$, and a compressible one, $\mathbf{u}_i^{(c)} \equiv \mathbf{u}_i^{(c)}(x,y,t)$, satisfying $\nabla\times\mathbf{u}_i^{(c)} = 0$. Therefore, with $\mathbf{u}_i(x,y,t) = \mathbf{u}_i^{(nc)}(x,y,t) + \mathbf{u}_i^{(c)}(x,y,t)$, the kinetic energies are split as

$$E_i^K(t) = E_i^{nc}(t) + E_i^c(t)$$
$$\equiv \frac{m_1}{2m_i}\int d^2\mathbf{r}\left[\left|\mathbf{u}_i^{(nc)}\right|^2 + \left|\mathbf{u}_i^{(c)}\right|^2\right]. \quad (10)$$

In 2D momentum space, with $\mathbf{k} = (k_x, k_y)$ and $d^2k = dk_x dk_y$, these two parts of the kinetic energies, with $(\alpha) \equiv (c), (nc)$, can be written as

$$E_i^{(\alpha)}(t) = \frac{m_1}{2m_i}\int d^2\mathbf{k}\left|\mathcal{F}_i^{(\alpha)}(\mathbf{k},t)\right|^2,$$
$$= \frac{m_1}{8\pi^2 m_i}\int d^2\mathbf{k}\left|\int d^2\mathbf{r}\, e^{-i\mathbf{k}\cdot\mathbf{r}}\mathbf{u}_i^{(\alpha)}\right|^2. \quad (11)$$

To analyze the contributions of sound waves as well as vortices, both compressible and incompressible parts of the kinetic energies are determined. The torque experienced by the time-dependent stirring potential, $V_s(r,\theta,t)$, which is given by Eq. (5), can be obtained through the corresponding torque operator,

$$\tau_z(\mathbf{r},t) = -\frac{\partial}{\partial\theta}V_s(r,\theta,t) = \epsilon\,r^2\sin(2\theta + 2\Omega_E t), \quad (12)$$

which corresponds to applying a rotation in the elliptical time-dependent part of the potential, with $2\Omega_E t \rightarrow 2\Omega_E t - \pi/2$. Due to this change in the time-dependent potential, it follows that the expected values of the induced angular momenta, $\langle L_z(t)\rangle_i$, and respective moment of inertia, $\langle I(t)\rangle_i$, are given

by

$$\langle L_z(t)\rangle_i = -i \int d^2r \; \psi_i^\star \frac{\partial}{\partial \theta} \psi_i \;\; \text{and} \;\; \langle I(t)\rangle_i = \int d^2r |\psi_i|^2 \; r^2,$$

with the associated classical rotational velocity being

$$\Omega_i(t) \equiv \frac{\langle L_z(t)\rangle_i}{\langle I(t)\rangle_i}. \tag{13}$$

We are aware that it is a nontrivial problem to calculate the moment of inertia of a superfluid or a condensate system. In the literature, the perturbation theory is commonly used to calculate the momentum of inertia for trapped ideal Bose gases. It is a temperature-dependent treatment, in which the condensed and noncondensed parts are considered in the calculation of the moment of inertia of a quantum system. Since we are working with a pure GP model, the noncondensate thermal clouds are not taken into account. We just use the classical relation to obtain approximate rotational velocities.

The structure factor provides us with information about the periodicity of the condensate density. For triangular lattice geometry, there are periodic peaks of regular hexagonal geometry. By looking at the position of peaks of the structure factor, we can distinguish between the Abrikosov lattice and the pinned vortex lattice.

We can also consider for the coupled system the density structure factor [60], which is a function of the $k \equiv \sqrt{k_x^2 + k_y^2}$ that provides information on the lattice order, the periodicity of the condensate density. This structure factor can be expressed by

$$s_i(k) = \frac{1}{2\pi} \int d^2r \; |\psi_i|^2 e^{-i\mathbf{k}\cdot\mathbf{r}}. \tag{14}$$

D. Kinetic energy spectrum in rotating frame

The rotating-frame velocity field, at a given frequency Ω, is defined by subtracting the corresponding rigid-body velocity field, as

$$\mathbf{v}_\Omega = \mathbf{v} - (\mathbf{\Omega} \times \mathbf{r})_z, \tag{15}$$

such that, for each density component n_i, the associated particle current $\mathbf{j}_{i,\Omega}(\mathbf{r},t) \equiv n_i(\mathbf{r},t)\mathbf{v}_{i,\Omega}(\mathbf{r},t)$ satisfies the continuity equation

$$\frac{\partial n_i(\mathbf{r},t)}{\partial t} + \nabla \cdot \mathbf{j}_{i,\Omega}(\mathbf{r},t) = 0. \tag{16}$$

Therefore, by following Eqs. (9)–(11), when considering a rotating frame at a given frequency Ω, we obtain

$$E_{i,\Omega}^{(\alpha)}(t) = \frac{m_1}{2m_i} \int d^2k \left| \mathcal{F}_{i,\Omega}^{(\alpha)}(\mathbf{k},t) \right|^2$$
$$\equiv \frac{m_1}{m_i} \int_0^\infty dk \; E_{i,\Omega}^{(\alpha)}(k,t), \tag{17}$$

which is defining the *velocity power spectral density* in k space as given by

$$E_{i,\Omega}^{(\alpha)}(k,t) = k \int_0^{2\pi} d\theta_k \left| \mathcal{F}_{i,\Omega}^{(\alpha)}(\mathbf{k},t) \right|^2. \tag{18}$$

Within this definition, for convenience, we are removing the relative mass ratio difference, which does not affect the

corresponding spectral behavior of each component. This equation is used to calculate the kinetic energy (or velocity) power spectra densities presented in this work. The computational methods for calculating the velocity power spectrum using decomposed kinetic energies are discussed in more detail in Ref. [61].

III. VORTEX FORMATION

In our study, we have considered two mass-imbalanced mixtures, such that we can contrast the results obtained by a mixture with a large mass difference between the components, given by ^{85}Rb - ^{133}Cs, with the results obtained by a system with a negligible mass difference, exemplified by ^{85}Rb - ^{87}Rb. Once stable lattice patterns are verified for both cases, averaged frequencies are derived from the results given by the stirring model, which is further considered to obtain the lattice patterns from the ground-state time-independent results.

Therefore, we split our results into two parts, corresponding to the two binary systems we are studying.

A. Binary ^{85}Rb - ^{133}Cs mixture

In this subsection, we are presenting the main results considering the binary mass-imbalanced system composed of the ^{85}Rb and ^{133}Cs. As previously stated, the sample results we have obtained are for fixed scattering lengths in a miscible configuration, such that $\delta = 0.5$. In view of the actual experimental control on the condensation of these two atomic species, we understand that Feshbach resonance techniques [58] can be considered to approximately bring the coupled system to this hypothetical condition. In Fig. 1, through the time evolution of the densities, we have the main results for the densities, in which the route to the vortex lattice generated by the stirring potential was shown. By considering four sets of panels, within the 2D space defined by the Cartesian coordinates (units of ℓ_ρ), we provide the results for the densities at some specific time intervals, characterizing specific regimes, for both ^{85}Rb (upper panels labeled 1) and ^{133}Cs (lower panels labeled 2) species. To obtain stable nonrotating ground-state solutions, we first solve the coupled Eq. (3) by using imaginary time ($t \to -it$), with $\epsilon = 0$ (without the stirring potential). Next, this ground-state solution is evolved in real time, by considering a rotating elliptical frequency $\Omega_E = 1.25$ with the strength of the stirring potential $\epsilon = 0.025$, as given in Eq. (5). The first coupled panels of Fig. 1, (a_1) and (a_2), are for $t = 200$, which refers to the time interval when shape deformations start to occur in the system. As verified, the condensed system is already displaying elliptical deformations (quadrupole excitations), due to the stirring potential, which periodically reverses back to the symmetric 2D trap, with the expected full cycle given by π/Ω_E. The shape deformation is more noticeable in the first lighter component (^{85}Rb) than in the second one (^{133}Cs). This periodic behavior goes on until a break occurs in the symmetry, with vortex nucleations happening at the surface of the condensed species, after enough long-time evolution ($t > 3000$). For this second interval, just before and at the time the nucleation of vortices starts to appear, we select two sets of plots in Fig. 1, for $t = 3600$ [panels (b_1) and (b_2)] and for $t = 4000$ [panels (c_1) and (c_2)].
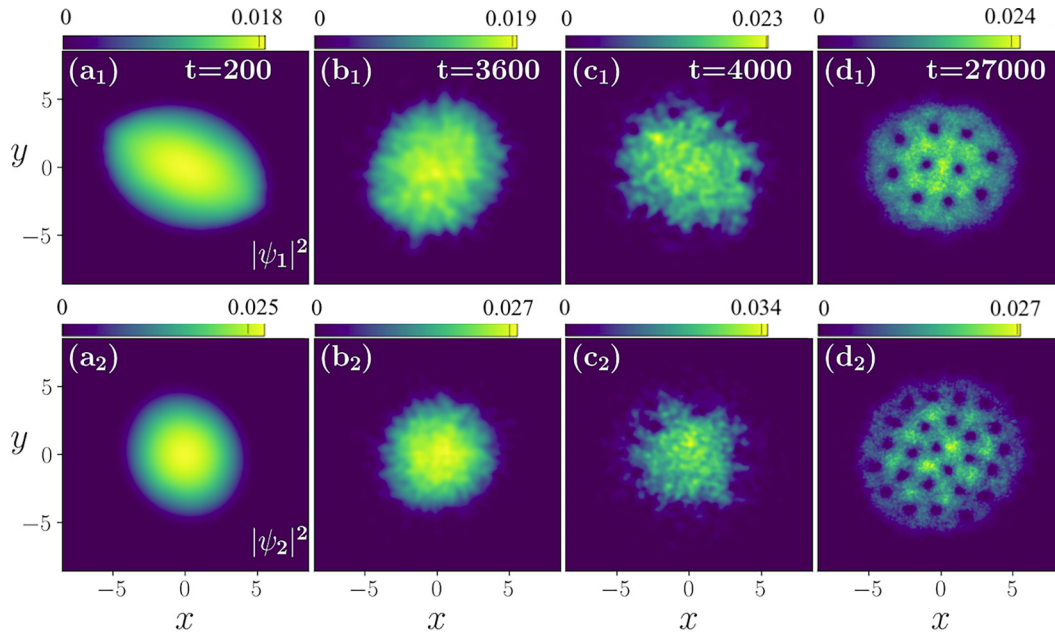
FIG. 1. Set of panels indicating the time evolution of the densities for the condensed mixture ^{85}Rb - ^{133}Cs in a miscible configuration with $\delta = 0.5$. The upper panels are for ^{85}Rb (component 1), with the lower panels for ^{133}Cs (component 2). By starting with a ground-state solution, the system is evolved in real-time with $\Omega_E = 1.25$ and $\epsilon = 0.025$. The density levels are indicated at the top of the panels. Within given units, all quantities are dimensionless.

The time interval in which we can observe the break in the symmetry is represented by the two sets of panels (b_i) and (c_i), within an interval of $\Delta t = 400$ (with $t = 3600$ and 4000). As the time increases, after an interval in which turbulent behaviors are verified, the nucleated vortices move from the surface to the inner part of the condensates, lattice patterns start appearing in both coupled condensates, and their positions become stable. At the final configuration, we noticed that the number of nucleated vortices emerging in the heavier component is significantly larger than the number of vortices obtained for the lighter species. The density evolutions represented in Fig. 1 can be better analyzed by considering the corresponding evolution of the associated kinetic energies, which are shown in Fig. 2 in the laboratory frame. For that, considering the two condensed species, the total kinetic energies are shown in Fig. 2(a), which are decomposed in two parts as shown in Fig. 2(b), one of which is compressible and the other incompressible. In the initial time interval, the energy oscillations correspond to the breathing mode oscillations of the condensates. The energies display increasing behaviors from the elliptical deformation phases of the condensates, returning to the established energies as they follow the trap symmetry. The shape deformation is more noticeable in the first component (^{85}Rb) than in the second one (^{133}Cs), which can be understood by the different inertia of the species. The increase of both component energies occurs due to the vortex nucleations. In this case, we observed that a more drastic increase is verified for the second, heavier one. At the final configuration, it is also noticed that the number of nucleated vortices emerging in the condensed heavier component is significantly larger than the lighter one. In general, the energies in the rotating frame decrease when the rotation frequency

or vortex number increases. The laboratory-frame continuous growth of the energies, verified even after saturation of the vortex number, is associated with the applied time-dependent stirring potential to a coupled system.

To analyze the different dynamical behaviors, one relevant observable is the kinetic energy, which we separate from the total energy. The kinetic energy is decomposed into two parts, considering the compressibility of each condensed part of the mixture. The behaviors of the total kinetic energies of both components are presented in Fig. 2(a), with the corresponding decomposition in compressible and incompressible parts shown in Fig. 2(b). The increase in the energies can be visually verified in the plots shown in Fig. 2, which become linear in the long time interval, as for $t > 10^4$. It is more significant to analyze the kinetic energy of the system to understand the vortex generation, because all the information about the velocity fields can be extracted from the associated kinetic energies, such as the elements related to sound-wave propagation and vortex generation. Therefore, it is appropriate to distinguish, in the total kinetic energy, the parts corresponding to acoustic wave propagations (compressible) from the ones related to vortex generation (incompressible). The total kinetic energy contribution has a similar oscillating behavior as the total energy in the initial time evolution, with huge energy contributions arising due to vortex and sound-wave productions along the long-time dynamical rotation. In this process, the main contributions in the kinetic energies will come from the incompressible energies, but significant contributions also from the compressible parts, as verified in Fig. 2(b). As compared with the total energy (not shown in the figure), we should point out that in the first stage of time evolution, before the nucleation of vortices, the kinetic energy is just a small fraction of the total energy, with the oscillating
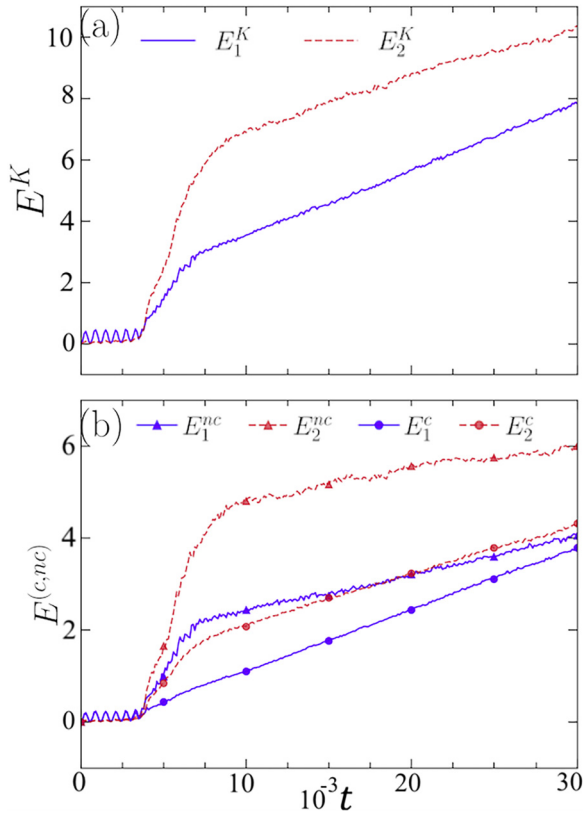
FIG. 2. For each component of the mixture, ^{85}Rb ($i = 1$, solid blue lines) and ^{133}Cs ($i = 2$, dashed red lines), the time evolutions are presented (in the laboratory frame) for (a) the kinetic energies, $E_i^K \equiv E_i^K(t)$, and (b) their corresponding compressible (E_i^c, indicated with bullets) and incompressible (E_i^{nc}, indicated with triangles) parts. With the initial configuration being ellipsoidal, the evolution is shown until stable vortex patterns are verified. Within given units, all quantities are dimensionless.

behavior stronger in the lighter component. However, in the longer time evolution, the total kinetic energy of the ^{133}Cs component grows to be more than 20% of the total energy, whereas the corresponding total kinetic energy increase of the ^{85}Rb element becomes near 16% of the total energy. This is consistent with the observed number of vortices emerging in the case of ^{133}Cs when compared with the corresponding number for the ^{85}Rb, as verified by the results given in Fig. 1.

The vortex nucleation responsible for the increase in the kinetic energies starts to occur at the surface, moving to the inner part of the condensates, with the incompressible parts providing the main contribution to the total kinetic energy. While comparing both components, the compressible and incompressible parts of the kinetic energy of the second component (^{133}Cs) are larger than the ones obtained for the first component (^{85}Rb), by a factor that, in a longer time interval, can be associated with the corresponding mass ratio between the two species. To improve our understanding of the dynamics of the vortex lattice formation from the rotating elliptical trap, in this case of a large mass-imbalanced mixture, we also plot the complete time evolution of the current density ($\mathbf{j} = n\mathbf{v}$) and corresponding torque for the two species until the vortex patterns are generated and become stable. The
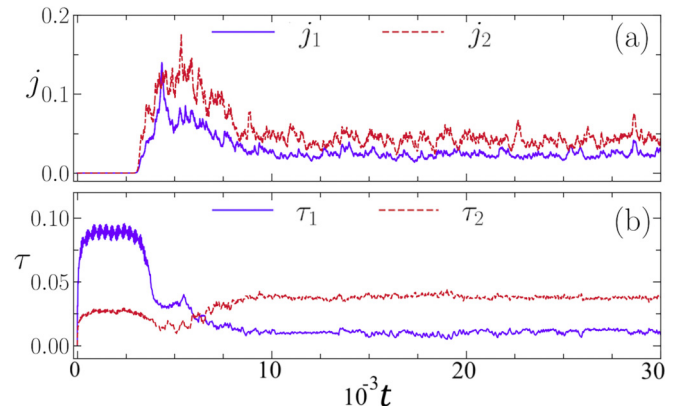

FIG. 3. For the ^{85}Rb ($i = 1$) and ^{133}Cs ($i = 2$) mixture, the respective time evolutions of the current densities [(a), given by (8)] and torques [(b), given by (12)] are shown until stable vortex patterns are verified. Within given units, all quantities are dimensionless.

results are presented in Fig. 3, with the current densities shown in Fig. 3(a), and the torques given in Fig. 3(b). As verified, in the initial evolution the current densities are zero for both components of the mixture, until a symmetry breaking occurs near $t \sim 3000$, with vortices being nucleated at the surface. The current densities reach their maxima around $t \sim 5000$, when the mixture is in a turbulent condition, decreasing to an average value consistent with the stabilization of the number of vortices being generated. Consistently, in all the time evolution, the current is higher for the more massive element of the mixture, the ^{133}Cs in the present case. This higher current is consistent with the larger number of vortices being generated.

In Fig. 3(b), in correspondence with Fig. 3(a), the torques experienced by both components due to the stirring potential are shown during the time evolution of the system. The time-dependent stirring trap potential provides the initial rotational energy for the system to rotate. This increase in the rotational energy is distributed between the two components, being more effective in the case of the lighter component, with the peak in the torque reaching its maximum in the time interval $t < 3000$. The heavier element, with corresponding higher inertia, is feeling an initial torque that is about 30% of the lighter one. However, in the longer time interval, with both averaged values varying close to fixed stable points, it is verified that the heavier element experiences higher torque than the lighter one. These results can be associated approximately with the number of vortices induced in the densities of both components shown in Fig. 1. The square root of the torque ratio is of the same order as the square of the mass ratios, and also the ratio between the number of vortices.

The time evolutions obtained for the classical rotational velocities $\Omega_i(t)$ are shown in Fig. 4, obtained from the expected value ratios between the induced angular momentum $\langle L_z \rangle_i$ and the corresponding momentum of inertia $\langle I \rangle_i$, as given by Eq. (13). The rotating condensates always reflect the angular momentum, which is a conserved quantity, at the equilibrium state. When the angular momentum of the system increases, the rotational velocity also increases correspondingly. We can clearly observe three time intervals in the evolution of the rotational velocity, given by Eq. (13), as indicated inside the
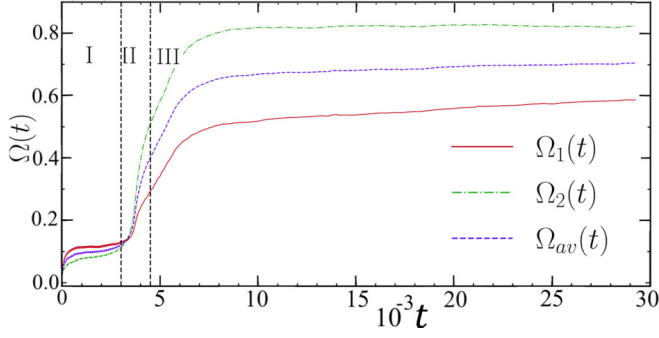
FIG. 4. Time evolutions of the rotational frequencies [Eq. (13)]: $\Omega_1(t)$, for ^{85}Rb (solid red line); $\Omega_2(t)$, for ^{133}Cs (dot-dashed green line), and with the corresponding averaging, $\Omega_{av}(t) \equiv [\Omega_1(t) + \Omega_2(t)]/2$ (dashed blue line). The vertical lines are approximately separating three time intervals: (I) shape deformations; (II) turbulent regime, with starting vortex nucleations; and (III) when vortex patterns are settled. Within given units, all quantities are dimensionless.

figure. The initial interval I corresponds to the period in which we have the shape deformations of the condensates. The nucleation of vortices occurs in the region identified by II in the figure, which corresponds to the increase of the velocities observed in Fig. 3(a). In region III, we have the vortex lattice formations, with $\Omega_i(t)$ converging to almost constant values.

The overall time evolution of the expected values will provide the corresponding time-dependent defined classical rotational frequency for each component of the mixture, given by a red solid line for the lighter species (^{85}Rb) and a green dot-dashed line for the heavier species (^{133}Cs). As shown in Fig. 4, the frequencies grow faster for the lighter component than for the heavier one in the initial time interval, when the coupled system is still in the time interval given by region I, before the nucleation of vortices. In region II, we notice the transition with vortices nucleation at the surface, when the frequencies start to grow faster for the heavier element. The stabilization of the frequencies, which happens faster for the larger mass component, is verified in the long time interval given by region III, with the emergence of stable vortex patterns.

In order to simulate the ground-state solution within a time-independent approach, as given by the replacement (6), we consider the frequency Ω_0 as corresponding to a time averaging of both rotational frequencies $\Omega_i(t)$, in which we assume for the total averaging time the interval from zero up to the point in which the frequency becomes almost constant, such that $\Omega_i(t \geqslant T) \approx \Omega_i(T)$. With this prescription, we obtain

$$\Omega_0 \equiv \frac{1}{T} \int_0^T \Omega_{av}(t) dt = \frac{1}{2T} \int_0^T [\Omega_1(t) + \Omega_2(t)] dt. \quad (19)$$

From the results shown in Fig. 4, in which $T \sim 30\,000$ and the saturated averaged frequency is $\Omega_{av}(T) \sim 0.72$, the above prescription will give us $\Omega_0 \sim 0.63$. As shown in Fig. 5, this prescription is providing an approximate good value for the classical rotational frequency, when used in Eq. (3), without the stirring potential.

In Fig. 5 we provide a comparison between the results for the coupled densities obtained with the stirring potential
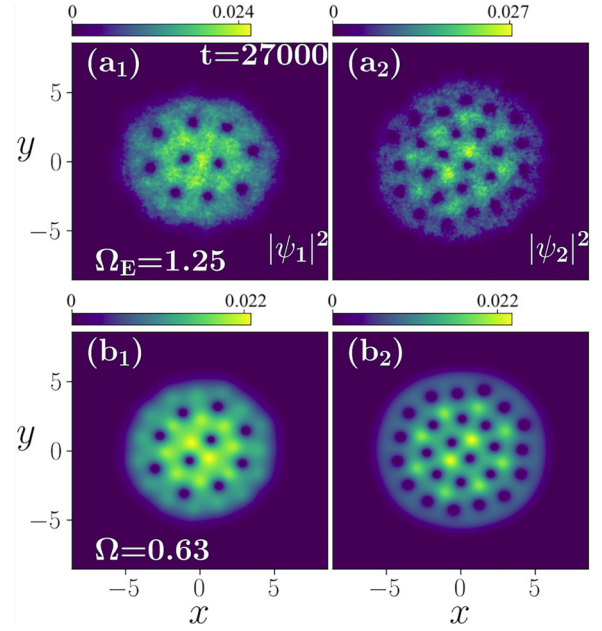

FIG. 5. Vortex-pattern solutions, obtained at $t = 27\,000$ with the stirring potential [$(a_i) = (d_i)$ of Fig. 1], are compared with ground-state solutions of Eq. (3), using (6) with $\Omega_0 = 0.63$ [shown in panels (b_i)]. The density levels are indicated at the top of each panel. Within given units, the plotted quantities are dimensionless.

[panels (a_i)] and without it [panels (b_i)] by using the prescription (19). By considering the laser stirring potential (5), with $\Omega_E = 1.25$ and $\epsilon = 0.025$, the corresponding stable results presented in panels (a_1) and (a_2) are the ones previously shown in panels (d_1) and (d_2) of Fig. 1, respectively, for $t = 27\,000$. Without the stirring potential, using (6), we obtain the complete ground-state solutions of the coupled densities by considering the frequency Ω_0 as given by the time averaging frequency (19), which will give us approximately $\Omega_0 = 0.63$ in the present case. The results verified in panels (b_1) and (b_2) of Fig. 5, computed directly for the ground-state solutions, as obtained for the ground-state solutions are not affected by sound-wave propagations. The correspondence between the density panels (a_i) with (b_i) was also confirmed by examining the lattice orders obtained from Eq. (14), with the structure factors providing good agreement on the associated peak positions.

B. Binary ^{85}Rb - ^{87}Rb mixture

For the case of two isotopes of the same species, we assume the binary mixture ^{85}Rb - ^{87}Rb. The main purpose of repeating the same kind of calculations previously done for the ^{85}Rb - ^{133}Cs is to verify clear mass-imbalance effects in our results. Particularly, we will try to point out the system which is more favorable in the production of vortex patterns by using a stirring potential. For that, we follow the previous same parametrizations for the trap and particle interactions, considering a complete miscible configuration, with $\delta = a_{12}/a_{11} = 0.5$ (where $a_{22} = a_{11} = 60a_0$).

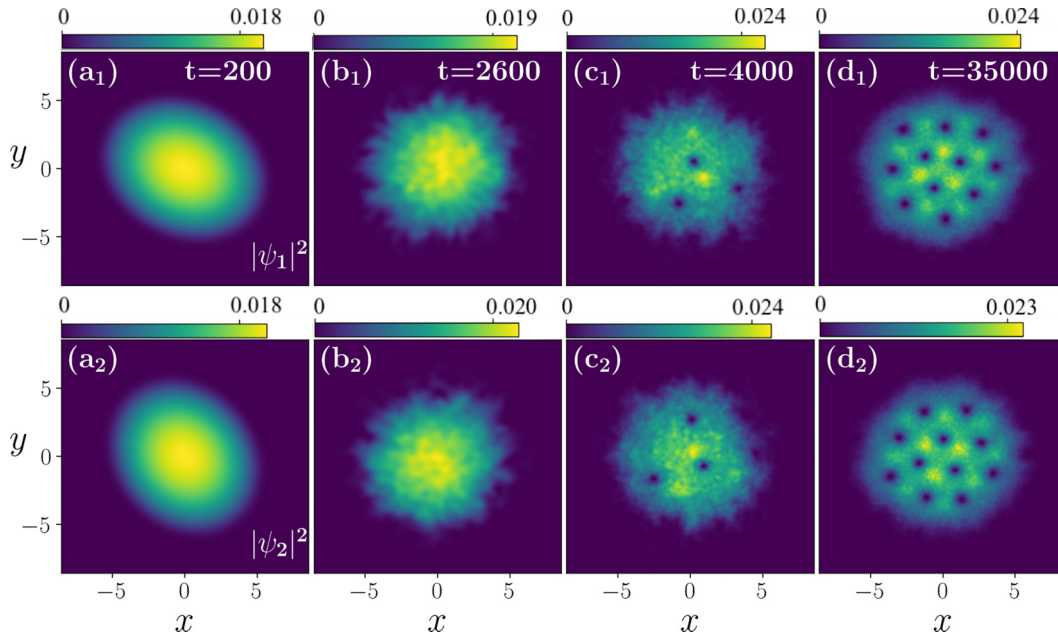The time evolution of the densities can be verified by the four sets of panels shown in Fig. 6, for the two species,

FIG. 6. Set of panels indicating the time evolution of the densities for the mixture ^{85}Rb - ^{87}Rb. The upper panels are for the ^{85}Rb (component 1), with the lower panels for ^{87}Rb (component 2). As in the case of Fig. 1, by starting with a ground-state solution, the system is evolved in real time with $\Omega_E = 1.25$ and $\epsilon = 0.025$. The density levels are indicated at the top of the panels. Within given units, the plotted quantities are dimensionless.

with the upper row being for the ^{85}Rb and the lower row for the ^{87}Rb. As expected, due to the small mass difference between the components, the dynamical behavior observed for both species is similar along the time evolution, until the vortex patterns become stable. In comparison with Fig. 1, we should observe that the time to reach the condition in which the surface nucleated vortices move from the surface to the inner part of the condensates is shorter. This behavior can better be verified by considering the results obtained for the other observables, in correspondence with the previous stronger mass-imbalanced case. For that, we are presenting the time-evolution results for the kinetic energies in Fig. 7, currents and torques in Fig. 8, with the corresponding classical rotational velocities shown in Fig. 9.

In this case, with both species having about the same mass, the final number of vortices verified for both components are the same, as shown in Fig. 6. Also as expected, the respective results are very close for the kinetic energies of both species, such that we are representing the total kinetic energies in Fig. 7(a), with the compressible and incompressible parts of the kinetic energies in Fig. 7(b). As in the case of the ^{85}Rb - ^{133}Cs considered in Fig. 2, initially the kinetic energies are a very small fraction of the total energy (not shown in the figure), becoming a large fraction (about 13%) of the total energy in the longer time propagation. These results, together with the results shown for the current and torques, are also quite in contrast with the corresponding ones verified for the stronger mass-imbalanced case, where the process of vortex nucleations and the movement to the inner part of the condensate becomes much faster. The time to stabilize the final vortex patterns is much longer in the case of close mass-imbalanced coupled systems, as one can verify in particular from the
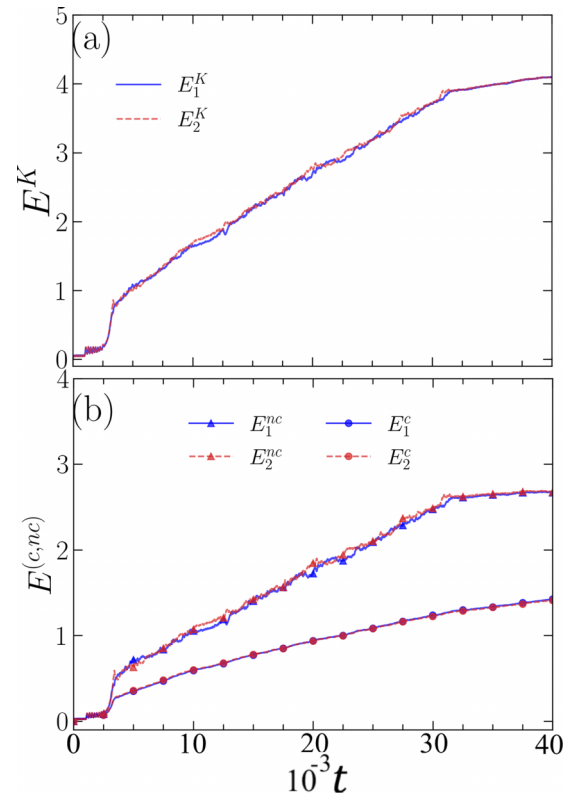

FIG. 7. For both components, ^{85}Rb ($i = 1$) and ^{87}Rb ($i = 2$), (a) shows the almost complete overlap of the total kinetic energies (solid blue for E_1^K, with dashed red for E_2^K). The compressible (bullets) and incompressible (triangles) parts of E_i^K are shown in (b). Within given units, all quantities are dimensionless.
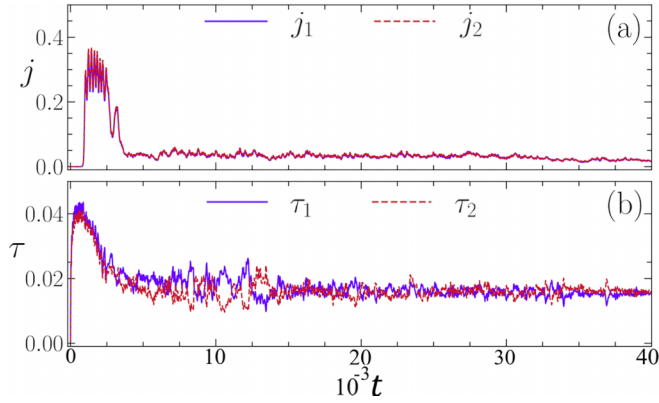
FIG. 8. The current densities (a) with the torques (b), respectively given by Eqs. (8) and (12) for both components, are shown for the ^{85}Rb - ^{87}Rb mixture, during the dynamical process that occurs until the vortex generation. Within given units, all quantities are dimensionless.

results obtained for the classical rotational frequencies. By comparing Fig. 9 with Fig. 4, we noticed that the averaged frequencies are already reaching convergence at $t \sim 30\,000$ for ^{85}Rb - ^{133}Cs. However, for ^{85}Rb - ^{87}Rb, a much longer time is needed for a final convergence.

In Fig. 10, we follow the same procedure done in Fig. 5 for ^{85}Rb - ^{133}Cs, now considering the almost identical mass system, ^{85}Rb - ^{87}Rb, by providing a comparison between the results for the coupled densities obtained with the stirring potential (using the same parameters $\Omega_E=1.25$ and $\epsilon = 0.025$) [panels (a_i)] and without it [panels (b_i)]. The corresponding stable results, presented in panels (a_1) and (a_2), are the ones previously shown in panels (d_1) and (d_2) of Fig. 6, respectively, for $t = 35\,000$. By using (6), i.e., removing the time-dependent perturbation, we obtain the complete ground-state solutions of the coupled densities with $\Omega_0 = 0.6$ in the lower panels. In this case, the prescription (19) gives a value for the frequency close to the asymptotic limit verified in
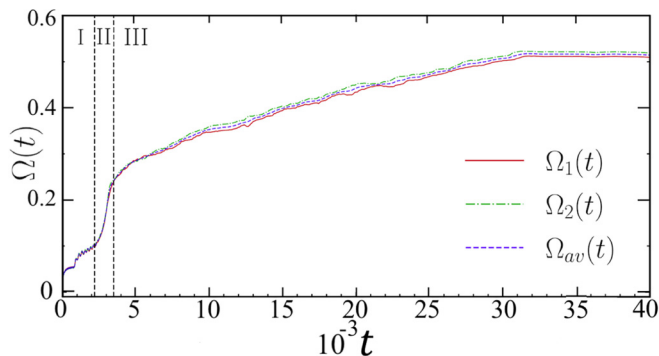

FIG. 10. Vortex-pattern results, at $t = 35\,000$ with the stirring potential [(a_i) = (d_i) of Fig. 6], are compared with ground-state solutions of Eq. (3), using (6) with $\Omega_0 = 0.6$ [panels (b_i)], for the coupled system ^{85}Rb (species 1) and ^{87}Rb (species 2) in miscible configuration $a_{12}/a_{11} = 0.5$. The density levels are indicated at the top of each panel. Within given units, all quantities are dimensionless.

Fig 9, $\Omega_{av} \approx 0.52$, pointing out a lower value for Ω_0 to improve the agreement between the density panels (a_i) and (b_i).

IV. INCOMPRESSIBLE KINETIC ENERGY SPECTRA

In this section, we consider the velocity power spectral densities in the k space, as given by Eqs. (17) and (18), for the analysis of the incompressible kinetic energy spectra of the two components, which is the more appropriate part of the kinetic energy concerned with the fluidity characteristics in the vortex production. The kinetic energy spectral methods for analyzing turbulent flows in symmetry-breaking quantum fluids within the Gross-Pitaevskii limit can be found in Ref. [61]. The incompressible $E^{(nc)}$ spectrum is expected to behave as k^{-3} when vortex configurations become well established inside the condensate. In the time evolution regime, before reaching the vortex-pattern configuration, the spectrum is expected to approach the $k^{-5/3}$ Kolmogorov behavior, characterizing the turbulent regime of a fluid. In order to enhance the effect of mass differences in this power-law dynamical behavior study, in the next, both behaviors of the mass-imbalanced coupled systems, ^{85}Rb - ^{133}Cs and ^{85}Rb - ^{87}Rb, will be analyzed comparatively along the time evolution of the mixtures. Therefore, in the next, both mass-imbalanced coupled systems, ^{85}Rb - ^{133}Cs and ^{85}Rb - ^{87}Rb, have their incompressible kinetic energy spectra, $E^{(nc)}(k, t)$, presented in Figs. 11 and 12. The results are displayed as functions of the wave number k multiplied by the corresponding healing lengths ξ. For both cases, in the selected set of coupled panels, we are considering time instants, with the corresponding classical rotational fre-

FIG. 9. Time evolution of $\Omega_i(t)$ [Eq. (13)] of both components, ^{85}Rb (solid red curve) and ^{87}Rb (dot-dashed green curve), with the corresponding averaged result, $\Omega_c(t) = [\Omega_1(t) + \Omega_2(t)]/2$ (dashed blue curve). Vertical lines are indicating three time intervals in the evolution: (I) shape deformations; (II) transition period with nucleation of vortices at the surface; and (III) with vortex lattices being formed. Within given units, all quantities are dimensionless.
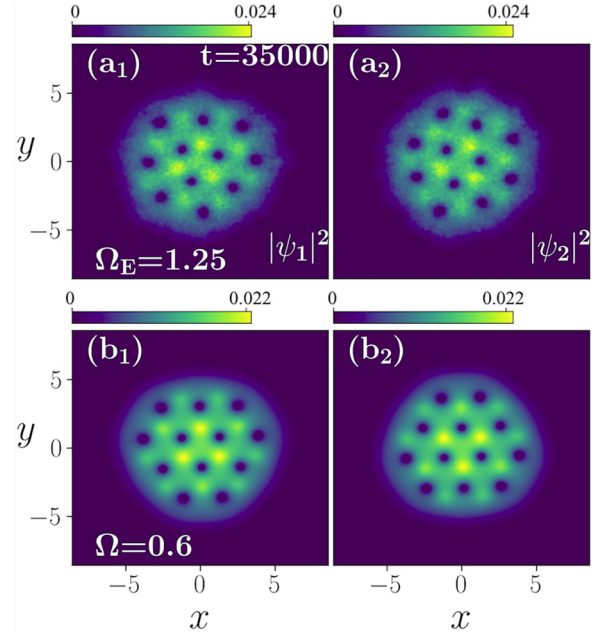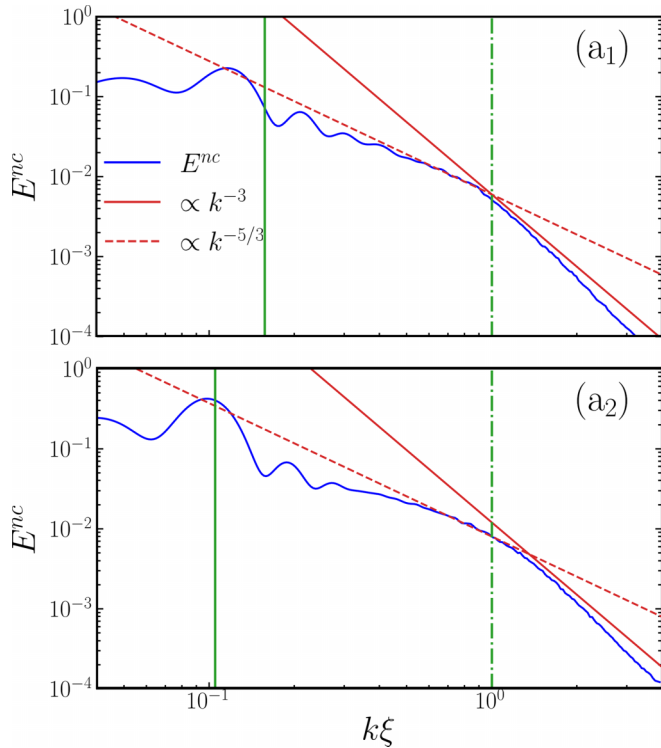
FIG. 11. Incompressible kinetic energy spectra, $E^{nc} \equiv E^{nc}(k,t)$, for the ^{85}Rb - ^{133}Cs mixture, obtained by averaging over 50 samples in the turbulent time interval (II) indicated in Fig. 4, which approximately agrees with the classical Kolmogorov $k^{-5/3}$ power-law behavior in the shown interval $0.1 < k\xi < 1$ (red dashed lines), being modified to the k^{-3} in the ultraviolet region. Within given units, all quantities are dimensionless.

FIG. 12. Incompressible kinetic energy spectra, $E^{nc} \equiv E^{nc}(k,t)$, for the ^{85}Rb - ^{87}Rb mixture, by averaging over 50 samples in the turbulent interval (II) indicated in Fig. 9. With behavior similar to the one observed for the stronger mass-imbalanced case in Fig. 11, the change in the power-law behavior is verified for larger values of $k\xi$. Within given units, all quantities are dimensionless.

quencies, which are representative of the time intervals before and after the nucleation of the vortices.

A. ^{85}Rb - ^{133}Cs kinetic energy spectra

We first examine the kinetic energy spectra for the case in which a stronger mass imbalance exists between the species. By considering the three regions defined in Fig. 4, we can select representative time intervals of the evolution. The first interval (I), also corresponding to panels (a$_i$) of Fig. 1, refers to the shape deformation interval, when we noticed that the rotation frequency is much slower for the heavier component. Since there is no vortex formation at this stage, analyzing the spectrum in this regime does not provide any useful information about power-law behavior. Also, in the last part of interval III, one should not expect any turbulent behavior, considering that the system is already close to equilibrium. As the system approaches this time interval, with a pattern of vortices already established, one should notice the characteristic power-law k^{-3} behavior, which is lost when sound waves start hassling the vortex cores.

Therefore, time interval II is the more relevant one in order to characterize the turbulent regime at which vortices start to be formed at the surface (near $t \sim 3500$–4000), entering the inner part of the condensates in the last part of the interval (when t is close to 4500). We consider this interval to examine in more detail the possible expected power-law
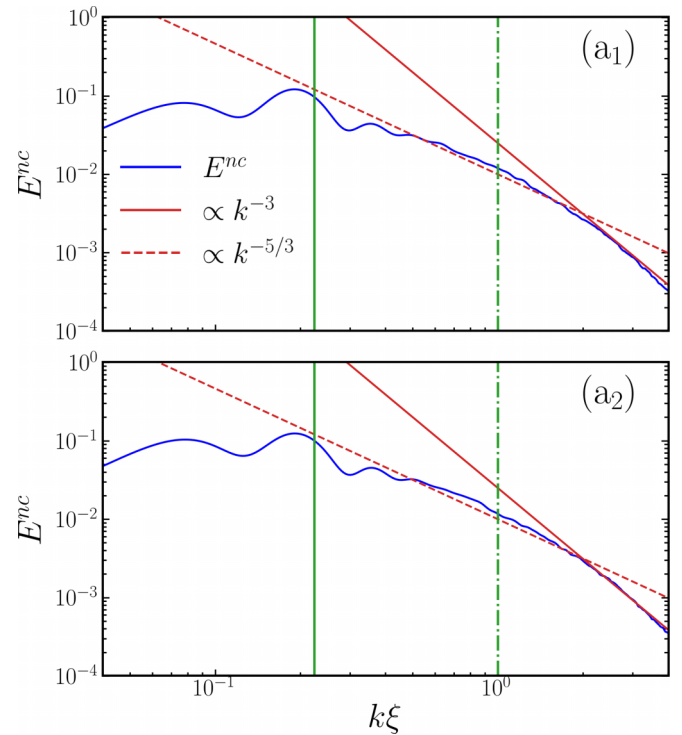
behavior. To better characterize this regime, going from turbulent to vortex pattern formation, in Fig. 11 we display the incompressible kinetic energy spectra for the two components of the ^{85}Rb - ^{133}Cs mixture, in terms of $k\xi$ (where ξ refers to the specific healing length of each condensate species). The results, obtained by averaging over 50 samples in the turbulent time interval II defined in Fig. 4, clearly confirm the Kolmogorov $k^{-5/3}$ power-law behavior in the turbulent regime II for $k\xi \lesssim 1$, which changes to k^{-3} for larger momenta.

Significantly, a quantum fluid is more turbulent at this stage due to a large number of vortex generations at the surface. The quantum fluid looks more turbulent until the torque, experienced by the condensates due to laser stirring, approaches the more stable region (as observed in Fig. 3). Along the process, the coupled condensates have a continuous energy injection due to the laser stirring potential. The velocity power spectrum is dominated by the rigid-body rotation spectrum in the infrared regime. In this work, we remove the large infrared contribution by calculating the spectrum in the rotating frame, as the amplitude of the infrared signal is greatly reduced in such a frame. The incompressible kinetic energy spectra, corresponding to the vortex configurations presented in panels (d$_i$) of Fig. 1, are shown over $k\xi$ in log scale. Similarly as in Ref. [19], also by considering our present results of coupled systems, the spectra are analyzed for the infrared ($k\xi \ll 2\pi$) and ultraviolet ($k\xi \gg 2\pi$) regimes. The incompressible spectrum becomes more important when vortices enter the system. In the ultraviolet regime, the incompressible kinetic energy

spectrum has a universal k^{-3} scaling behavior that arises from the vortex core structure. In the infrared regime, the incompressible spectrum is in agreement with the Kolmogorov $k^{-5/3}$ power law. This power-law feature is kept until $k\xi \sim 2\pi$, changing to k^{-3} at higher momenta. These behaviors vanish after the vortices have entered the inner part of the densities, with the coupled system relaxing to the crystallization of lattice patterns.

B. ^{85}Rb - ^{87}Rb kinetic energy spectra

By following a similar analysis as done in the previous section for ^{85}Rb - ^{133}Cs, in Fig. 12 we have our results for the spectra when considering the ^{85}Rb - ^{87}Rb mixture. For this mixture, the corresponding density distributions are given in Fig. 6. In this case, following the same order as before, we have the initial shape deformation interval being represented in (a_i), at $t = 200$. The other time instants are for the time interval when the nucleation of vortices starts $[(b_i)$, at $t = 2600]$, entering the inner part $[(c_i)$, at $t = 4000]$, and when the vortex patterns become stable $[(d_i)$, at $t = 35\,000]$.

As we have considered before, for this system we are also focusing in particular on region II, indicated in Fig. 9, where the turbulent regime occurs, until patterns of vortices are formed for each component. The corresponding results are shown in Fig. 12, with the upper panel showing the spectra for the component ^{85}Rb and the lower panel for the component ^{87}Rb. Again, our results were obtained by averaging over 50 samples in region II, considering the fixed time intervals. In comparing the two kinds of mixtures, we observe that the Kolmogorov $k^{-5/3}$ power-law behavior in the turbulent regime II (verified for $k\xi \lesssim 1$) is shifted to larger values of $k\xi$ when considering close mass differences between the species. We also observe the same kind of change happening for the k^{-3} behavior, which starts for larger values of $k\xi$.

V. CONCLUSIONS

We have studied the vortex nucleation dynamics and associated turbulent flows produced by elliptical laser stirring of two kinds of mass-imbalanced coupled Bose-Einstein condensates confined to an effective two-dimensional pancake geometry. We modeled two easily accessible and controllable systems in cold-atom experiments: mixtures of ^{85}Rb - ^{133}Cs and ^{85}Rb - ^{87}Rb, both in the miscible regime.

During stirring, we observed the stages of instability known in the single-component system [18]: shape deformation, symmetry breaking involving vortex nucleation, and finally the approach to rotating frame equilibrium. To characterize vortex nucleation in the coupled BEC system, we computed the time evolution of relevant dynamical observables for each of the two components of the mixture, including the total and kinetic energies, the current densities, and torques.

During the shape deformation regime, the kinetic energy injected is primarily compressible, switching to incompressible energy when vortex nucleation begins. For low mass imbalance, the final vortex lattices are similar, while for the high mass imbalance system the heavier species support more vortices at the same rotation frequency. This is consistent with

the Feynman rule for the vortex density in a rigidly rotating lattice [13], while in the vortex density is proportional to the atomic mass.

The initial torque experienced by the coupled condensates soon after switching on the laser stirring is stronger for the less-massive atomic species. When vortices approach stabilized lattice configurations, for both elements the torques saturate, being stronger for the more massive one. To calculate the effective time-dependent rotational frequency of each component, we used the classical rotational relation obtained from the expected values of the angular momenta and moment of inertia operators. The larger mass-imbalanced mixture has a larger rotational frequency than the lower mass-imbalanced mixture. This is also reflected in the visible number of vortices shown in the final vortex lattice.

As a measure of vortex energy, we compute the incompressible kinetic energy, taking care to subtract the uninteresting rigid body velocity field associated with the rotation. In the turbulent regime, the incompressible kinetic energy shows some evidence of a Kolmogorov $k^{-5/3}$ scaling, for values of the k momenta (as a function of the inverse of healing lengths ξ^{-1}) smaller than 1, which is modified to a k^{-3} power-law behavior in the ultraviolet regime determined by the vortex core structure [19]. While the Kolmogorov scale range is somewhat limited, the spectrum is consistent with energy transport to large scales as disordered vortices enter the system and begin to organize. The vortices in this stage are close to the boundary of the condensate, and the Kolmogorov power-law scaling vanishes once stable vortex configurations develop.

Comparing the large and small mass-imbalance systems reveals two notable features. First, we noticed that a large mass-imbalance system shows the approximate $k^{-5/3}$ power-law behavior for a longer time window. In this regard, see Figs. 11 and 12, in which one can also notice that the change in the scaling behavior, from $k^{-5/3}$ to k^{-3}, occurs at lower incompressible kinetic energies for larger mass differences between the species. Second, the dynamical production of stable patterns of vortices is verified to be a much faster process for larger mass-imbalanced systems than for smaller mass-imbalanced ones.

In addition to the above outcomes, we should also point out that, in the case where a single condensate is confined under the same stirring interaction conditions (implying no interparticle interactions, or $g_{12} = 0$), the process of production of a stable pattern of vortices will be much faster. These results may impact experimental investigations in which equal or nearly equal two-particle masses are considered in miscible (with $g_{12} \neq 0$) configurations, such as when two spinor components of the same atom are being studied in condensed cold-atom experiments. The other extreme, with much larger mass-imbalanced miscible mixtures being considered, is also of interest, considering that faster production of stable patterns can be achieved. Finally, from another perspective, the present study for coupled condensates, under stirring potential, can be extended by using damped Gross-Pitaevskii analysis, with a treatment of the condensates with their corresponding thermal components. It can be useful to calculate precisely the effective rotational velocity of the thermal clouds.

[1] M. R. Matthews, B. P. Anderson, P. C. Haljan, D. S. Hall, C. E. Wieman, and E. A. Cornell, Vortices in a Bose-Einstein Condensate, Phys. Rev. Lett. **83**, 2498 (1999).

[2] K. W. Madison, F. Chevy, W. Wohlleben, and J. Dalibard, Vortex Formation in a Stirred Bose-Einstein Condensate, Phys. Rev. Lett. **84**, 806 (2000).

[3] F. Chevy, K. W. Madison, and J. Dalibard, Measurement of the Angular Momentum of a Rotating Bose-Einstein Condensate, Phys. Rev. Lett. **85**, 2223 (2000).

[4] B. P. Anderson, P. C. Haljan, C. E. Wieman, and E. A. Cornell, Vortex Precession in Bose-Einstein Condensates: Observations with Filled and Empty Cores, Phys. Rev. Lett. **85**, 2857 (2000).

[5] K. W. Madison, F. Chevy, V. Bretin, and J. Dalibard, Stationary States of a Rotating Bose-Einstein Condensate: Routes to Vortex Nucleation, Phys. Rev. Lett. **86**, 4443 (2001).

[6] E. Hodby, G. Hechenblaikner, S. A. Hopkins, O. M. Maragò, and C. J. Foot, Vortex Nucleation in Bose-Einstein Condensates in an Oblate, Purely Magnetic Potential, Phys. Rev. Lett. **88**, 010405 (2001).

[7] J. R. Abo-Shaeer, C. Raman, J. M. Vogels, W. Ketterle, Observation of vortex lattices in Bose-Einstein condensates, Science **292**, 476 (2001).

[8] G. P. Bewley, D. P. Lathrop, and K. R. Sreenivasan, Visualization of quantized vortices, Nature (London) **441**, 588 (2006).

[9] E. J. Yarmchuk, M. J. V. Gordon, R. E. Packard, Observation of Stationary Vortex Arrays in Rotating Superfluid Helium, Phys. Rev. Lett. **43**, 214 (1979).

[10] R. J. Donnelly, *Quantized Vortices in Helium II* (Cambridge University Press, Cambridge, 1991).

[11] M. Tsubota, K. Kasamatsu, and M. Kobayashi, Quantized vortices in superfluid helium and atomic Bose-Einstein condensates, in *Novel Superfluids*, edited by K. H. Bennemann and J. B. Ketterson (Oxford Univ. Pr., Oxford, 2013), Vol. 1, Chap. 3, p. 156.

[12] M. Tsubota, M. Kobayashi and H. Takeuchi, Quantum hydrodynamics, Phys. Rep. **522**, 191 (2013).

[13] A. L. Fetter and A. A. Svidzinsky, Rotating trapped Bose-Einstein condensates, J. Phys.: Condens. Matter **13**, R135 (2001).

[14] M. W. Zwierlein, J. R. Abo-Shaeer, A. Schirotzek, C. H. Schunck, and W. Ketterle, Vortices and superfluidity in a strongly interacting Fermi gas, Nature (London) **435**, 1047 (2005).

[15] N. R. Cooper, Rapidly rotating atomic gases, Adv. Phys. **57**, 539 (2008).

[16] I. Bloch, J. Dalibard, and W. Zwerger, Many-body physics with ultracold gases, Rev. Mod. Phys. **80**, 885 (2008).

[17] A. L. Fetter, Rotating trapped Bose-Einstein condensates, Rev. Mod. Phys. **81**, 647 (2009).

[18] N. G. Parker and C. S. Adams, Emergence and Decay of Turbulence in Stirred Atomic Bose-Einstein Condensates, Phys. Rev. Lett. **95**, 145301 (2005).

[19] A. S. Bradley and B. P. Anderson, Energy Spectra of Vortex Distributions in Two-Dimensional Quantum Turbulence, Phys. Rev. X **2**, 041001 (2012).

[20] M. T. Reeves, B. P. Anderson, and A. S. Bradley, Classical and quantum regimes of two-dimensional turbulence in trapped Bose-Einstein condensates, Phys. Rev. A **86**, 053621 (2012).

[21] M. T. Reeves, T. P. Billam, B. P. Anderson, and A. S. Bradley, Signatures of coherent vortex structures in a disordered 2D quantum fluid, Phys. Rev. A **89**, 053631 (2014).

[22] T. P. Billam, M. T. Reeves, B. P. Anderson, and A. S. Bradley, Onsager-Kraichnan Condensation in Decaying Two-Dimensional Quantum Turbulence, Phys. Rev. Lett. **112**, 145301 (2014).

[23] G. Gauthier, M. T. Reeves, X. Yu, A. S. Bradley, M. Baker, T. A. Bell, H. Rubinsztein-Dunlop, M. J. Davis, and T. W. Neely, Giant vortex clusters in a two-dimensional quantum fluid, Science **364**, 1264 (2019).

[24] M. C. Tsatsos, P. E. S. Tavares, A. Cidrim, A. R. Fritsch, M. A. Caracanhas, F. E. A. dos Santos, C. F. Barenghi, and V. S. Bagnato, Quantum turbulence in trapped atomic Bose-Einstein condensates, Phys. Rep. **622**, 1 (2016).

[25] L. Madeira, M. A. Caracanhas, F. E. A. dos Santos, and V. S. Bagnato, Quantum turbulence in quantum gases, Annu. Rev. Condens. Matter Phys. **11**, 37 (2020).

[26] L. Madeira, A. Cidrim, M. Hemmerling, M. A. Caracanhas, F. E. A. dos Santos, and V. S. Bagnato, Quantum turbulence in Bose-Einstein condensates: Present status and new challenges ahead, AVS Quantum Sci. **2**, 035901 (2020).

[27] J. Amette Estrada, M. E. Brachet and P. D. Mininni, Turbulence in rotating Bose-Einstein condensates, Phys. Rev. A **105**, 063321 (2022).

[28] M. Ghosh Dastidar, S. Das, K. Mukherjee, and S. Majumder, Pattern formation and evidence of quantum turbulence in binary Bose-Einstein condensates interacting with a pair of Laguerre-Gaussian laser beams, Phys. Lett. A **421**, 127776 (2022).

[29] S. Das, K. Mukherjee, and S. Majumder, Vortex formation and quantum turbulence with rotating paddle potential in a two-dimensional binary Bose-Einstein condensate, Phys. Rev. A **106**, 023306 (2022).

[30] C. J. Pethick and H. Smith, *Bose-Einstein Condensation in Dilute Gases* (Cambridge University Press, Cambridge, 2002).

[31] P. M. Stevenson, How do sound waves in a Bose-Einstein condensate move so fast? Phys. Rev. A **68**, 055601 (2003).

[32] R. K. Kumar, T. Sriraman, H. Fabrelli, P. Muruganandam, and A. Gammal, Three-dimensional vortex structures in a rotating dipolar Bose-Einstein condensate, J. Phys. B: At. Mol. Opt. Phys. **49**, 155301 (2016).

[33] R. P. Feynman, in *Progress in Low Temperature Physics*, edited by D. F. Brewer, Vol. 1, Chap. II, Application of Quantum Mechanics to Liquid Helium (North-Holland, Amsterdam, 1955).

[34] A. A. Abrikosov, On the magnetic properties of superconductors of the second group, Sov. Phys. JETP **5**, 1174 (1957) [Zh. Eksp. Teor. Fiz. SSSR **32**, 1442 (1957)].

[35] A. A. Abrikosov, Nobel Lecture Type II superconductors and the vortex lattice, Rev. Mod. Phys. **76**, 975 (2004).

[36] P. K. Newton and G. Chamoun, Vortex lattice theory: A Particle interaction perspective, SIAM Rev. **51**, 501 (2009).

[37] C. J. Myatt, E. A. Burt, R. W. Ghrist, E. A. Cornell, and C. E. Wieman, Production of Two Overlapping Bose-Einstein Condensates by Sympathetic Cooling, Phys. Rev. Lett. **78**, 586 (1997).

[38] P. Maddaloni, M. Modugno, C. Fort, F. Minardi, and M. Inguscio, Collective Oscillations of Two Colliding Bose-Einstein Condensates, Phys. Rev. Lett. **85**, 2413 (2000).

[39] T. Lahaye, C. Menotti, L. Santos, M. Lewenstein, and T. Pfau, The physics of dipolar bosonic quantum gases, Rep. Prog. Phys. **72**, 126401 (2009).

[40] J. P. Burke, J. L. Bohn, B. D. Esry, and C. H. Greene, Prospects for Mixed-Isotope Bose-Einstein Condensates in Rubidium, Phys. Rev. Lett. **80**, 2097 (1998).

[41] G. Modugno, M. Modugno, F. Riboli, G. Roati, and M. Inguscio, Two Atomic Species Superfluid, Phys. Rev. Lett. **89**, 190404 (2002).

[42] G. Ferrari, M. Inguscio, W. Jastrzebski, G. Modugno, G. Roati, and A. Simoni, Collisional Properties of Ultracold K-Rb Mixtures, Phys. Rev. Lett. **89**, 053202 (2002).

[43] G. Thalhammer, G. Barontini, L. De Sarlo, J. Catani, F. Minardi, and M. Inguscio, Double Species Bose-Einstein Condensate with Tunable Interspecies Interactions, Phys. Rev. Lett. **100**, 210402 (2008).

[44] S. B. Papp, J. M. Pino, and C. E. Wieman, Tunable Miscibility in a Dual-Species Bose-Einstein Condensate, Phys. Rev. Lett. **101**, 040402 (2008).

[45] D. J. McCarron, H. W. Cho, D. L. Jenkin, M. P. Köppinger, and S. L. Cornish, Dual-species Bose-Einstein condensate of ^{87}Rb and ^{133}Cs, Phys. Rev. A **84**, 011603(R) (2011).

[46] B. Pasquiou, A. Bayerle, S. M. Tzanova, S. Stellmer, J. Szczepkowski, M. Parigger, R. Grimm, and F. Schreck, Quantum degenerate mixtures of strontium and rubidium atoms, Phys. Rev. A **88**, 023601 (2013).

[47] L. Wacker, N. B. Jørgensen, D. Birkmose, R. Horchani, W. Ertmer, C. Klempt, N. Winter, J. Sherson, and J. J. Arlt, Tunable

[48] F. Wang, X. Li, D. Xiong, and D. Wang, A double species ^{23}Na and ^{87}Rb Bose-Einstein condensate with tunable miscibility via an interspecies Feshbach resonance, J. Phys. B: At. Mol. Opt. Phys. **49**, 015302 (2016).

[49] A. Trautmann, P. Ilzhöfer, G. Durastante, C. Politi, M. Sohmen, M. J. Mark and F. Ferlaino, Dipolar Quantum Mixtures of Erbium and Dysprosium Atoms, Phys. Rev. Lett. **121**, 213601 (2018).

[50] G. Natale, R. M. W. van Bijnen, A. Patscheider, D. Petter, M. J. Mark, L. Chomaz and F. Ferlaino, Excitation Spectrum of a Trapped Dipolar Supersolid and Its Experimental Evidence, Phys. Rev. Lett. **123**, 050402 (2019).

[51] R. M. Wilson, S. Ronen and J. L. Bohn, Stability and excitations of a dipolar Bose-Einstein condensate with a vortex, Phys. Rev. A **79**, 013621 (2009).

[52] R. M. Wilson, C. Ticknor, J. L. Bohn and E. Timmermans, Roton immiscibility in a two-component dipolar Bose gas, Phys. Rev. A **86**, 033606 (2012).

[53] X.-F. Zhang, L. Wen, C.-Q. Dai, R.-F. Dong, H.-F. Jiang, H. Chang, and S.-G. Zhang, Exotic vortex lattices in a rotating binary dipolar Bose-Einstein condensate, Sci. Rep. **6**, 19380 (2016).

[54] R. K. Kumar, P. Muruganandam, L. Tomio and A. Gammal, Miscibility in coupled dipolar and non-dipolar Bose-Einstein condensates, J. Phys. Commun. **1**, 035012 (2017).

[55] R. K. Kumar, L. Tomio, B. A. Malomed, and A. Gammal, Vortex lattices in binary Bose-Einstein condensates with dipole-dipole interactions, Phys. Rev. A **96**, 063624 (2017).

[56] R. K. Kumar, L. Tomio, and A. Gammal, Vortex patterns in rotating dipolar Bose-Einstein condensate mixtures with squared optical lattices, J. Phys. B: At. Mol. Opt. Phys. **52**, 025302 (2019).

[57] R. K. Kumar, L. Tomio, and A. Gammal, Spatial separation of rotating binary Bose-Einstein condensates by tuning the dipolar interactions, Phys. Rev. A **99**, 043606 (2019).

[58] E. Timmermans, P. Tommasini, M. Hussein, and A. Kerman, Feshbach resonances in atomic Bose-Einstein condensates, Phys. Rep. **315**, 199 (1999).

[59] R. Kishor Kumar, V. Lončar, P. Muruganandam, S. K. Adhikari, and A. Balaž, C and Fortran OpenMP programs for rotating Bose-Einstein condensates, Comput. Phys. Commun. **240**, 74 (2019).

[60] T. Sato, T. Ishiyama, and T. Nikuni, Vortex lattice structures of a Bose-Einstein condensate in a rotating triangular lattice potential, Phys. Rev. A **76**, 053628 (2007).

[61] A. S. Bradley, R. K. Kumar, S. Pal, and X. Yu, Spectral analysis for compressible quantum fluids, Phys. Rev. A **106**, 043322 (2022).